Functional Magnetic Resonance Imaging with Intermolecular Double-Quantum Coherences at 3 T

Andreas Schäfer,[1]* Thies H. Jochimsen,[1] and Harald E. Möller[1,2]

Functional magnetic resonance imaging (fMRI) based on the selection of intermolecular double-quantum coherences (iDQC) was performed with a standard birdcage coil at 3 T in a group of normal human volunteers. Suppression of spurious signal contributions from unwanted coherence-transfer pathways was achieved by combining a two-step phase cycle and a long repetition time of 5 s. A gradient-recalled echo iDQC sequence (echo time, T_E = 80 ms) yielded robust activation with a visual paradigm. Maximum *z*-scores were about half of those observed with conventional blood-oxygen level dependent fMRI, whereas the functional signal change increased by more than a factor of 5. No activation was obtained with a spin-echo iDQC sequence (T_E = 160 ms), in which dephasing accumulated during the evolution period was fully rephased by an appropriate delay time. It is hypothesized that substantial inherent diffusion weighting of the iDQC technique efficiently suppresses intravascular contributions to the functional contrast. A consistent quantitative explanation of the observed amount of signal change currently remains speculative. Magn Reson Med 53: 1402–1408, 2005. © 2005 Wiley-Liss, Inc.

Key words: BOLD contrast; dipolar interaction; fMRI; intermolecular double-quantum coherence (iDQC); phase cycling; signal stability

The possibility of generating contrast in magnetic resonance imaging (MRI) from intermolecular multiple-quantum coherence (iMQC) was introduced about a decade ago (1–4). Straightforward analysis shows that dipolar couplings, which directly act through space, can cause the transformation of multiple-spin coherences between separate molecules into observable magnetization (i.e., single-spin, single-quantum coherences [SQC]) (5). Within the traditional framework of liquid-state NMR theory, iMQCs are not observed. This is due to the fact that short-range dipolar interactions average to zero in time through rapid molecular tumbling, and long-range dipolar interactions average to zero in space in a magnetically isotropic sample. However, a magnetic field gradient can break this isotropy, and intermolecular dipolar couplings can reappear. An important feature of this effect is that its length scale is set by the applied gradient. Specifically, a "correlation gradient" of amplitude G_c and duration T winds up a magnetization helix and, hence, spatially modulates the sample. The bulk of the iMQC signal comes from spins that are separated by roughly the "correlation distance" which is defined by one half pitch of the helix, $d_c = (\pi/\gamma G_c T)$, and the amplitude depends on both the number of interacting spins and the sample heterogeneity on a dimension defined by d_c (2). This distance (and hence, contrast) can be tuned externally by the experimenter to a specific, mesoscopic length scale (between about 10 μm and 1 mm), which can be substantially smaller than a typical imaging voxel. This unique feature along with an increased sensitivity to the local magnetic susceptibility distribution has driven recent interest in iMQC in the context of MRI.

Previous applications include imaging of rat (3,6) and cat brain (7), human brain (6,8–14) and extremities (10), as well as experimental tumor (3), trabecular bone (15,16), and motion-insensitive diffusion-weighted imaging (17). According to their coherence order, p, intermolecular double-quantum coherences (iDQCs) precess at twice the Larmor frequency and are thus more sensitive to local magnetic susceptibility variations than the conventional SQC signal. This has already been used to generate a strong blood-oxygen level dependent (BOLD) contrast for functional MRI (fMRI) (8,11,12), whereas the proposed possibility to tailor the distance scale of the BOLD sensitivity to blood vessels of a specific size for optimum specificity (i.e., by adjusting the correlation gradient accordingly) remains to be shown experimentally.

A serious limitation for iMQC imaging is, however, its intrinsically poor signal-to-noise ratio (SNR), which is roughly an order of magnitude below that of conventional MRI. Thorough optimization of the imaging sequence is thus of paramount importance. To overcome the SNR penalty, previous single-subject fMRI experiments based on iDQC have either used an ultrahigh magnetic field strength of 7 T (8) or relied on local surface coils for optimizing the sensitivity in a specific brain area, such as the visual cortex (8) or the auditory cortex (11,12). The latter approach is, however, impractical if whole-brain coverage is needed. The objective of the present work was to evaluate the feasibility of iDQC-based fMRI with a standard volume head coil at a moderate field strength of 3 T, which is increasingly becoming available. Similar to previous work, we combined the "COSY revamped with asymmetric *z*-gradient echo detection" (CRAZED) pulse sequence originally introduced by Warren et al. (1) with an echo-planar imaging (EPI) readout (18) to achieve iDQC imaging with sufficient temporal resolution for fMRI. Both gradient-recalled echo (GRE) and spin-echo (SE) acquisition schemes are compared in normal human volunteers using visual stimulation. Finally, hypotheses about potential contributions to the observed functional signal change are discussed.

METHODS

All experiments were carried out at 3 T (Magnetom Trio, Siemens, Erlangen, Germany) with the standard head coil

[1]Max Planck Institute for Human Cognitive and Brain Sciences, Leipzig, Germany.

[2]Department of Radiology, University Hospital Münster, Münster, Germany.

*Correspondence to: Andreas Schäfer, Max Planck Institute for Human Cognitive and Brain Sciences, Stephanstrasse 1a, D-04103 Leipzig, Germany. E-mail: schaefer@cbs.mpg.de

Received 1 November 2004; revised 17 January 2005; accepted 18 January 2005.

DOI 10.1002/mrm.20506

Published online in Wiley InterScience (www.interscience.wiley.com).

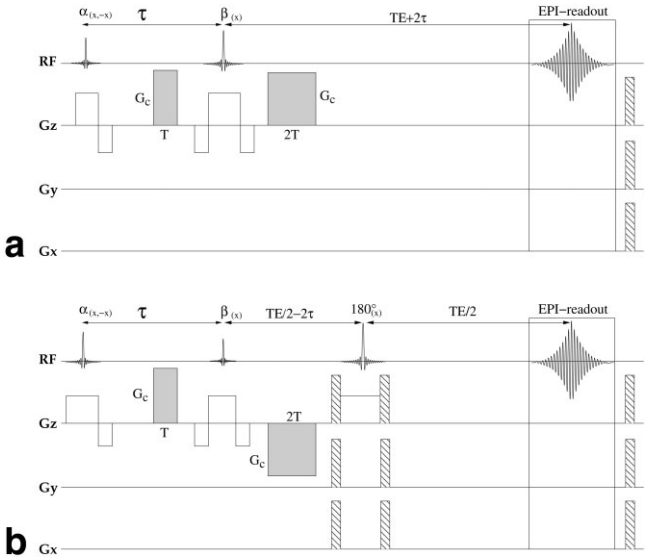

FIG. 1. GRE-iDQC (**a**) and SE-iDQC (**b**) pulse sequences. For simplicity, the read and phase-encoding gradients of the EPI readout are omitted. The double-quantum gradient filter consisting of two gradient pulses with a ratio of 1:2 for the first gradient moment is marked in gray. The polarity of the second iDQC selection gradient is reversed in the SE-iDQC sequence to select the $p = -2$ coherence. After the acquisition, remaining magnetization is spoiled by crusher gradients.

(birdcage design) being used for radiofrequency (RF) excitation and signal acquisition. The gradient system was capable of producing a maximum gradient amplitude of 40 mT/m along each axis of the laboratory coordinate system within a minimum rise time of approximately 200 μs.

The ODIN framework was used for sequence programming (19). Modified CRAZED pulse sequences for generating iDQC contrast are shown in Fig. 1. An initial pulse with flip angle $\alpha = 90°$ generates two-spin iMQCs from quadratic terms in the equilibrium density matrix (besides conventionally observed one-spin SQC), which evolve during the evolution period of duration τ and pass a double-quantum gradient filter (20) that eliminates all but the iDQCs. The β pulse transforms iDQC into two-spin SQC, which is finally converted during the detection period by dipolar couplings into observable magnetization to form a coherence-transfer echo after a delay time, $T_D = p\tau$, following the β pulse (here $p = \pm 2$). This dipolar signal is spatially encoded by an EPI gradient scheme, either directly in the GRE-iDQC sequence (Fig. 1a) or after a 180° refocusing pulse in the SE-iDQC sequence (Fig. 1b). To achieve maximum signal intensity, the flip angle of the β pulse was set to 120° (for the $p = +2$ coherence) or 60° (for the $p = -2$ coherence) in case of the GRE-iDQC and SE-iDQC sequence, respectively, in accordance with density-matrix calculations (4,21).

The amplitude and duration of the correlation gradient were set to $G_c = 22$ mT/m and $T = 3.4$ ms to achieve a correlation distance of $d_c \approx 160$ μm. An evolution time of $\tau = 10$ ms was used throughout. Marques and Bowtell (22) have shown that the sensitivity to signal changes caused by small variations in T_2 is maximized by setting an echo time $T_E = 2T_2$ in the SE-iDQC sequence. Long echo times of 80 and 160 ms were therefore used in the functional study for the GRE-iDQC and SE-iDQC sequences, respectively. The repetition time was set to $T_R = 5$ s, and the acquisition bandwidth of the EPI readout was $B_W = 65$ kHz. In the fMRI studies, a two-step phase cycle ($\alpha_x\ \beta_x$, $\alpha_{-x}\ \beta_x$) along with receiver phase (x, x) was used, and adjacent data pairs of the time series (i.e., images 1 + 2, 2 + 3, ..) were added in k-space prior to image reconstruction.

Prior to the in vivo study, initial experiments were performed on a spherical water phantom (aqueous solution of 4.76 mmol/L $NiSO_4$) of 16-cm inner diameter to verify the authenticity of the iDQC signal. It is well known that the iMQC signals scale with the second-order Legendre polynomial, $3\cos^2\theta - 1$, due to the underlying dipolar couplings (23). θ is the angle between the directions of the main magnetic field, $\mathbf{B}_0$, and the correlation gradient. By contrast, the intensity of a conventional SQC signal does not depend on the gradient direction. Image intensities measured with the SE-iDQC sequence ($T_R = 5$ s, $T_E = 80$ ms, $B_W = 100$ kHz, 2 acquisitions) in an axial slice through the phantom at different angles between 0 and 90° are plotted in Fig. 2. As predicted for the dipolar signal, maximum intensity is obtained at $\theta = 0°$, half maximum intensity at $\theta = 90°$, and zero intensity at the magic angle ($\theta = 54.7°$). In subsequent in vivo experiments, a short test scan in which the correlation gradient was applied at the magic angle was always performed to verify the absence of signal at the center of k-space.

For further investigation of the amount of potential contamination from unwanted coherences, a four-step phase cycle (α_x, α_{-x}, α_y, α_{-y}) was applied to the GRE-iDQC and SE-iDQC sequences (same parameters as in fMRI studies), and the signal intensity at the center of k-space was measured in axial, sagittal, and coronal slices through the

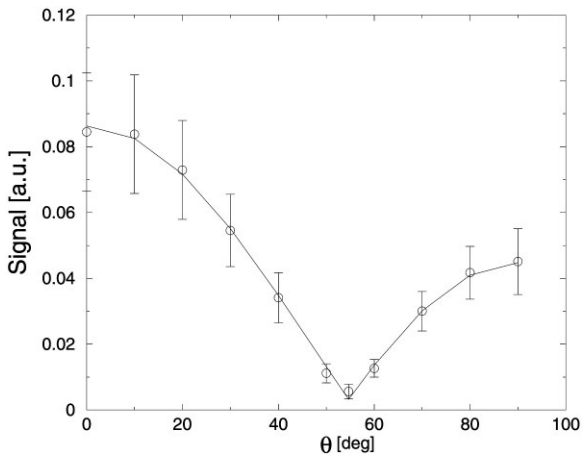

FIG. 2. Verification of the authenticity of the dipolar signal in a phantom experiment with the SE-iDQC sequence. In each image, a circular region of interest (ROI) of the size of the phantom was selected. Plots of the signal intensity measured at different angles θ (circles) are shown along with a fit to the function $S_0\,|3\cos^2\theta - 1| + N$ (solid line), where S_0 is the signal amplitude at $\theta = 0°$ and N denotes the noise level. The error bars indicate the SD of the signal intensity within the ROI.

Table 1
Receiver Phases of the Four-Step Phase Cycling Scheme for Different Coherence-Order Selection

Coherence order	Receiver phase
±2	(*x, x, −x, −x*)
0	(*x, x, x, x*)
+1	(*x, −x, −y, y*)
−1	(*x, −x, y, −y*)

phantom (16). The phases of the other pulses were held constant, $\phi_\beta = \phi_{180°} = (x)$. To select signal evolving with coherence order $p = 0$ (zero-quantum coherence [ZQC]), +1 (SQC), −1 (SQC), and ±2 (DQC), the receiver phase was cycled in a series of experiments as summarized in Table 1. Results are presented in Fig. 3, demonstrating that contributions from unwanted coherence pathways are of the order of the noise level. This indicates that the double-quantum gradient filter is highly efficient for selecting the desired iDQC signal.

A total of six healthy subjects (three female, 23–30 years old), who had given informed prior consent, were examined by fMRI. Five slices (thickness 5 mm, spacing 1 mm) were positioned parallel to and containing the calcarine fissure to cover the visual cortex. The field of view was 192 mm, and the matrix was 48 × 48 yielding a voxel size of 4 × 4 × 5 mm^3. For comparison, conventional BOLD experiments were additionally performed with $T_R = 2$ s and $T_E = 40$ or 80 ms with GRE-EPI or SE-EPI, respectively ($B_W = 100$ kHz). Prior to the functional experiments, 2D T_1-weighted images were acquired with the same geometry as anatomic reference using a power-reduced variant of the modified driven-equilibrium Fourier-transform (MDEFT) sequence (24).

In the iDQC experiments, visual stimulation was achieved by presenting a pattern of randomly rotating L-shape red objects for 30 s after a period of rest of the same duration. This block was repeated 13 times per trial. The stimulus was provided through a commercial goggle system (Resonance Technology, Northridge, CA, U.S.A.). For the conventional BOLD experiments, the same visual stimulation task was used, however, with stimulus and resting periods of 22 s and only six repetitions per trial. A total of three functional runs were performed per subject: In all six subjects, GRE-iDQC and SE-iDQC sequences were used along with conventional GRE-BOLD (three subjects) or SE-BOLD (three subjects) experiments. The order of the sequences was randomized among subjects to account for potential habituation effects.

The LIPSIA software package (25) was employed for evaluating the fMRI images. Postprocessing included spatial filtering with a Gaussian kernel of 0.6 voxels standard deviation (SD). A high-pass filter with a cut-off at one quarter of the total time steps was applied in the time domain to remove large-scale signal drifts. To align the functional data slices onto a 3D stereotactic reference system, a rigid linear registration with six degrees of freedom (three rotational, three translational) was performed. The rotational and translational parameters were obtained on the basis of the 2D MDEFT images to achieve an optimal match between these slices and an individual 3D reference scan acquired during a previous session using a magnetization-prepared rapid gradient echo sequence (26). The 3D volume data set with an isotropic resolution of 1 mm was standardized to the Talairach stereotactic space. The rotational and translational parameters were transformed by linear scaling and then used to transform the functional slices by trilinear interpolation.

Statistical analysis was based on a least-squares estimation using the general linear model for serially autocorrelated observations (27). The design matrix was generated with a boxcar function convolved with the hemodynamic response function. The model equation including the observation data, the design matrix, and the error term was convolved with a Gaussian kernel of dispersion 4-s full width at half maximum. The contrast between the differ-

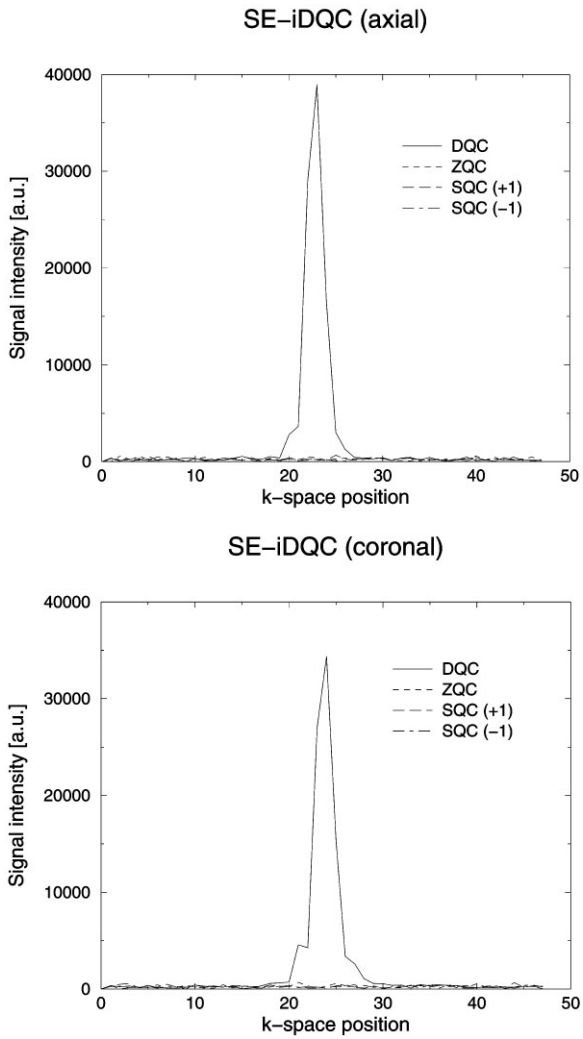

FIG. 3. Central *k*-space line along the phase direction measured with the SE-iDQC sequence in a water phantom with a four-step phase cycle and receiver phase according to Table 1 to select different coherence orders. Three different slice orientations were measured (only axial and coronal orientations are shown as representative examples). While a strong signal is obtained when selecting the iDQC, the intensity for other coherence pathways (ZQC, ±SQC) is of the order of the noise level. Identical results were obtained with the GRE-iDQC sequence (not shown).

Table 2
Signal Fluctuations during 60 Time Steps Measured in a Healthy Subject at Rest

T_R (s)	SD (%)
2	12
3	7.3
4	3.1
5	2.2
6	1.5

ent conditions was calculated on the basis of a t test. Subsequently, t values were transformed to z scores. The threshold in all functional maps was set to $z > 3.09$ ($P < 0.001$).

RESULTS

In time series, such as those used in fMRI, major spurious signal contributions may arise from interscan stimulated echoes (STEs) for which the signal excited in the first scan is refocused during the acquisition period of the second scan. Following the coherence-transfer pathway generating a "shifted STE," the magnetization is stored along the longitudinal axis between successive sequence repetitions, and hence, crusher gradients after the acquisition window are ineffective to remove such signal contributions. A thorough investigation of shifted STEs compared to the iMQC signals has been published by Mori et al. (7). To study the potential amount of this type of instability, time series consisting of 60 repetitions were recorded with the GRE-iDQC sequence (T_E = 80 ms, two-step phase cycle) in vivo in a volunteer at rest. The observed SD of the scan-to-scan variation of the signal intensity (average of the center slice measured with a magnitude mask) is summarized in Table 2 for various repetition times between 2 and 6 s. Additionally, a series of 60 repetitions was recorded with a conventional GRE-EPI sequence (T_R = 2 s as typically used in fMRI) using a low RF pulse flip angle of 2° to adjust the signal to a similar amplitude as obtained with the iDQC sequence. A 0.9% SD was obtained for this reference scan. As can be seen from Table 2, an increased signal stability toward the level of the reference scan was obtained with increasing T_R. A relatively long T_R of 5 s was therefore chosen in the fMRI experiments to achieve sufficiently robust conditions.

A summary of the fMRI results (z-maps superimposed on anatomic T_1-weighted images) is presented in Fig. 4. One representative slice per subject is shown for conventional GRE- or SE-BOLD, GRE-iDQC, and SE-iDQC imaging. All acquisitions with conventional BOLD-based fMRI as well as with GRE-iDQC fMRI showed activated voxels, which were well contained in the visual cortex. By contrast, no activation was recorded using the SE-iDQC sequence and an identical threshold ($z > 3.09$). Quantitative results are summarized in Table 3. The number of activated voxels detected by GRE-iDQC was smaller compared to both GRE-BOLD and SE-BOLD. A high percentage of the activated voxels detected with GRE-iDQC was commonly activated with GRE-BOLD (84%) or SE-BOLD (75%). Consistent with previous observation, significantly increased

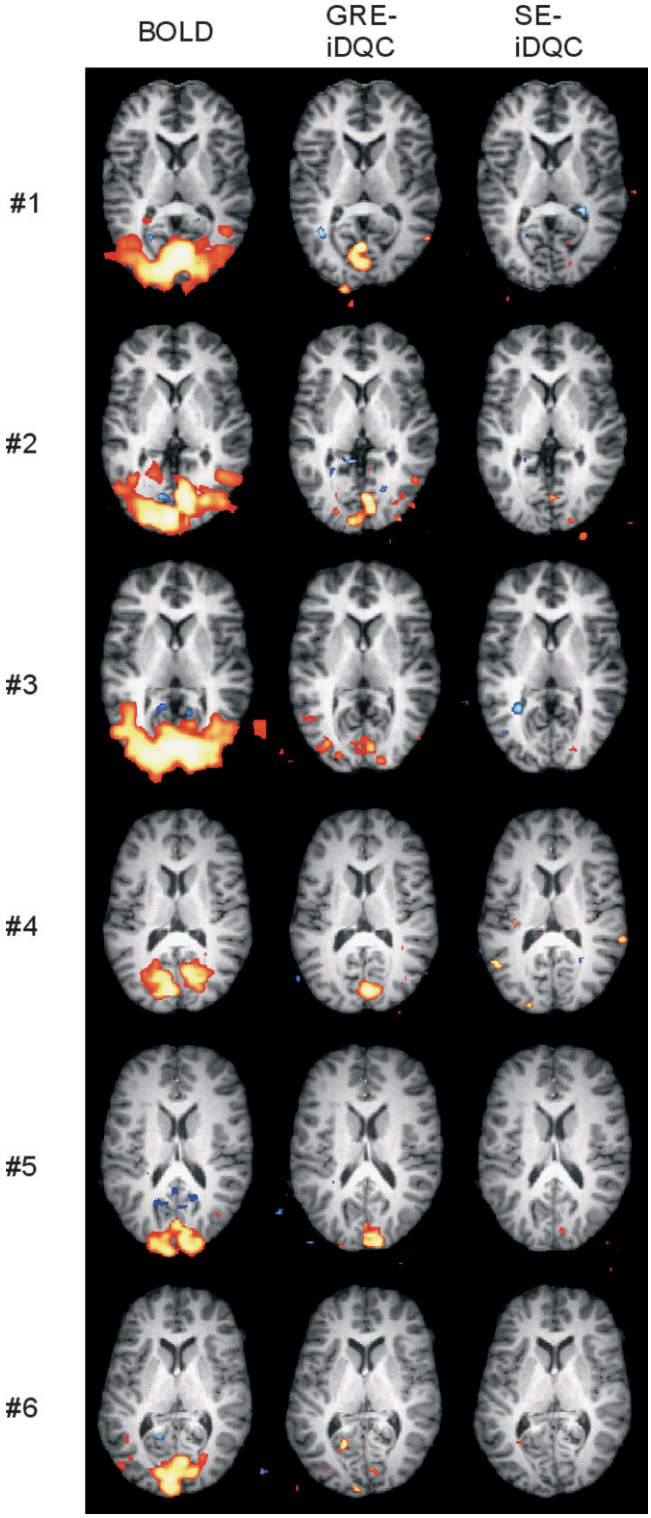

FIG. 4. Functional maps recorded with a blocked visual paradigm in all six subjects. The first column shows conventional BOLD images (lines 1–3 acquired with GRE-EPI and T_E = 40 ms and lines 4–6 with SE-EPI and T_E = 80 ms). Results obtained in the identical subjects with the GRE-iDQC and SE-iDQC sequence are given in the second and third columns, respectively.

Table 3
Percentage Signal Change, Maximum *z*-Scores, and Number of Activated Voxels in the Visual Cortex Obtained with the Different fMRI Techniques (GRE-BOLD, SE-BOLD, GRE-iDQC) as Shown in Fig. 4

Subject	Signal change (%)		z_{max}		Number of activated voxels	
	BOLD	iDQC	BOLD	iDQC	BOLD	iDQC
1	1.9[a]	10.7	14.61	6.17	1182	132
2	1.9[a]	10.1	13.70	7.16	1536	108
3	1.8[a]	9.7	15.53	6.80	1475	184
4	1.8[b]	13.3	12.41	7.69	331	143
5	1.7[b]	12.9	11.24	6.53	296	38
6	1.7[b]	14.6	9.62	5.22	320	44
Mean	1.87 ± 0.06[a]	11.9 ± 2.0	14.61 ± 0.92[a]	6.60 ± 0.85	1398 ± 216[a]	108 ± 76
	1.73 ± 0.06[b]		11.1 ± 1.4[b]		316 ± 20[b]	

[a]GRE-BOLD fMRI.
[b]SE-BOLD fMRI.

percentage signal changes were found with multiple-quantum imaging, which were approximatly 1.9% for GRE-BOLD, 1.7% for SE-BOLD, and 11.9% for GRE-iDQC. An example of averaged GRE-BOLD and GRE-iDQC time courses is given in Fig. 5. As the iDQC experiment was measured with a poor temporal resolution of $T_R = 5$ s and a two-step phase cycle, reliable indications of a different peak position or significant deviations from the assumed hemodynamic response function are not obtained. Note that the relatively coarse resolution may produce some partial voluming. Such partial-volume effects might be more pronounced in the conventional BOLD approach where contrast is a simple average over all contributions within a voxel whereas iDQC imaging reflects subvoxel structure.

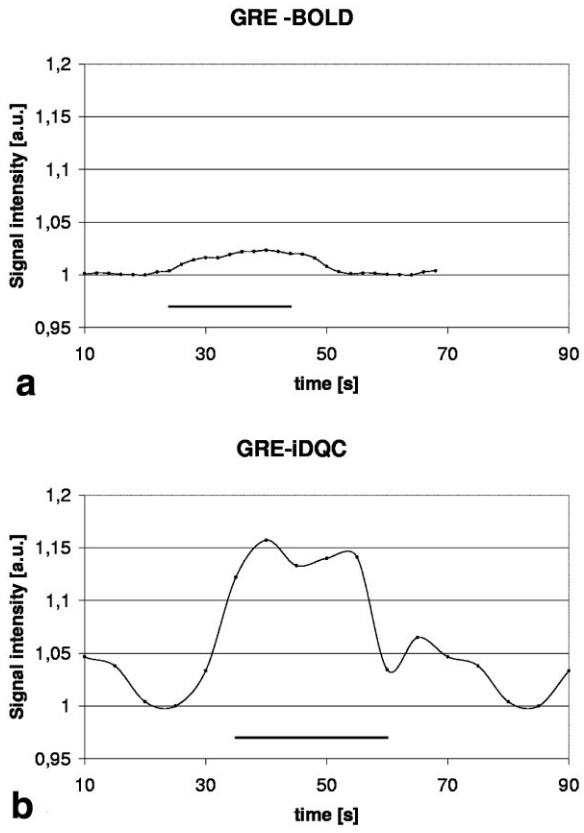

FIG. 5. Averaged time courses recorded under visual stimulation with GRE-BOLD (**a**) or GRE-iDQC (**b**) in subject 1. Raw signal time courses acquired over all stimulus/rest blocks of each series were averaged. Signal changes are approximately 1.9% for GRE-BOLD and 10.7% for GRE-iQDC.

DISCUSSION

The preparatory experiments on phantoms and a human volunteer show that the double-quantum gradient filter adjusted for a moderate correlation distance, $d_c = 160$ μm, reliably selects the desired coherence-transfer pathway as long as T_R is relatively long (> 4 s). Under such conditions, a two-step phase cycle is sufficient to suppress spurious signal contributions from SQC and ZQC. Upon reducing T_R, unwanted contributions from shifted STEs, which are generated from two successive repetitions of an iDQC sequence, were insufficiently suppressed. Resulting artifacts render the obtained stability of time series inappropriate for fMRI. If we consider that STEs are acquired with a mixing time, $T_M = T_R - \tau$ (compare Fig. 1), their amplitude will be reduced by a factor $\exp(-T_M/T_1)$ due to T_1 relaxation. With $T_1 = 1330$ ms for human cortical gray matter at 3 T (28), this reduction factor becomes approximately 2% with $T_R = 5$ s, and STE contributions are suppressed well below the level of the iDQC signal amplitude. Although somewhat higher signal fluctuations may be tolerated with iDQC-based fMRI compared to standard BOLD experiments in view of a more than fivefold increase of the functional signal change (Table 3 and Fig. 5), a relatively poor time resolution was, hence, required to achieve sufficient signal stability. An additional minor benefit from prolonging T_R might be some SNR enhancement as previous in vitro studies suggest that it takes longer for the iDQC signal to return to equilibrium in comparison to SQC (29).

Still open are questions about the spatial specificity of the functional contrast and its relation to the site of neuronal activation. Magnetic resonance angiography in one subject (data not shown) did not indicate a simple topographic relation between the pattern of functional iDQC

contrast and macroscopically visible veins. Compared to standard GRE- and SE-BOLD experiments, fewer activated voxels were found with the GRE-iDQC technique. It is tempting to hypothesize that this might be an effect of a more specific localization of activation achieved by the multiple-quantum technique (e.g., due to selecting a specific correlation distance). However, this observation might only reflect a threshold problem due to a reduced sensitivity of the iDQC experiment as maximum *z*-scores with GRE-iDQC were roughly half of those in the conventional BOLD experiments (Table 3). Further investigations are needed for clarification of this issue.

With T_R = 5 s, robust activation was reproducibly observed with the GRE-iDQC sequence (T_E = 80 ms), whereas no activated voxels were detected with the SE-iDQC sequence (T_E = 160 ms) despite an almost identical SNR of the individual images obtained with both sequences. In previous auditory studies, Zhong et al. (11,12) reported the observation of activation with an SE-iDQC sequence at 1.5 T. As no delay (i.e., $T_D = 0$) was used in these experiments, we may regard their approach as an "asymmetric SE-iDQC" sequence with remaining sensitivity to T_2* decay (predominantly during the evolution period). This contribution is, however, also detected with a GRE-iDQC approach, and choice of an asymmetric SE-iDQC technique does not seem to provide extra information. For separating T_2 effects, a delay $T_D = -2\tau$ (for the $p = -2$ coherence) after the β pulse (or, equivalently, adding a 180° pulse at the center of the evolution period) is needed to refocus the echo exactly at the center of *k*-space. Consistent with our results, functional contrast was lost after allowing a delay $T_D = p\tau$ to obtain a "symmetric SE-iDQC" sequence in Ref. (12). Note that we did not systematically vary τ and, hence, cannot exclude the possibility that sufficient BOLD sensitivity to detect activation with a symmetric SE-iDQC sequence may result when using longer evolution times.

The activation patterns obtained under visual stimulation in this work are qualitatively different from the sparse distribution of isolated foci of activation reported from a previous iDQC study at 7 T (8), in which a correlation distance of 100 μm was used with visual stimulation by flashing red LEDs. As currently comparative studies at different field strength are missing, it remains to be shown whether differences in $\mathbf{B}_0$ or sequence parameters (e.g., T_E or τ) might lead to qualitatively different activation patterns.

In conventional BOLD experiments, dynamic averaging in the intravascular proton pool accounts for a substantial contribution to the functional contrast at 3 T (30). Microcirculatory flow through a network of randomly oriented vascular segments may be modeled as a pseudodiffusion process (31–33), and it is well known that diffusion-weighting gradient schemes effectively suppress intravascular BOLD signal contributions (34,35). In iDQC imaging, incoherent spin motion blurs the spatial modulation of the magnetization and destroys the dipolar field, which offsets proper refocusing of transverse magnetization (17,36,37). Similarly, laminar flow was also recently shown to produce substantial signal reduction (38). Quantitative analysis of the effects from incoherent motion in CRAZED sequences indicates that the amount of diffusion weighting is a function of the correlation distance and the echo time. Kennedy and Zhong (17) suggested the computation of a *b*-factor according to $b_{iDQC} = \pi^2 T_E / d_c^2$ to characterize diffusion weighting due to the coherence selection gradients, which underlines that the role of T_E in iDQC imaging is similar to that of the diffusion time, Δ, in a standard Stejskal–Tanner experiment. This definition yields b_{iDQC} = 30.8 and 61.7 s/mm^2 with our experimental parameters for the GRE-iDQC and SE-iDQS sequence, respectively. Compared to this result, the additional diffusion weighting due to the spoiler gradients of the 180° refocusing pulse in the SE-iDQC sequence (Fig. 1b) is negligible (b = 1.8 s/mm^2). Recent SE-BOLD experiments using the same visual paradigm demonstrated that a *b*-factor of 50 s/mm^2 is sufficient to suppress nearly all of the intravascular signal at 3 T (30). Even though the diffusion weighting achieved with a given b_{iDQC} might be slightly overestimated (17), it seems reasonable to assume that most of the intravascular signal is lost due to the inherent diffusion weighting of the iDQC sequences.

Considering the combined effects from diffusion weighting and the potential spatial selectivity of the correlation distance of 160 μm we may hypothesize that the functional iDQC contrast primarily comes from the extravascular space. In conventional BOLD-fMRI, this length scale is probed more efficiently by GRE techniques being sensitive to susceptibility perturbers of all sizes whereas SE sequences are more sensitive to small-scale susceptibility compartments. Consistently, Fig. 4 indicates that the percentage of commonly activated voxels was greater when comparing GRE-iDQC with GRE-BOLD than with SE-BOLD. The above scenario would also explain the failure to detect activated voxels by SE-iDQC imaging. As the design of our SE-iDQC sequence accounts for a delay, $T_D = -2\tau$, static dephasing (T_2* effects) should not contribute to the signal, whereas functional contrast from dynamic averaging (T_2 dephasing) is potentially detectable at an appropriate T_E. As outlined above, extravascular dynamic averaging is much more pronounced around capillaries where variations in the local field strength occur on a relatively small spatial scale. This scale might not be probed efficiently when using d_c = 160 μm as in our experiments.

CONCLUSION

Our visual study demonstrates the feasibility to obtain robust activation in normal subjects with iDQC-based fMRI at 3 T using a standard RF volume coil. Excellent suppression of spurious signal contributions from unwanted coherence-transfer pathways is achieved with a simple two-step phase cycle and a relatively long T_R. Compared with standard BOLD-based fMRI, there is a substantial reduction in the SNR of the individual images, which is in part compensated by a more than fivefold increase in the functional signal change. At present, a precise statement about the origin of the functional contrast cannot be derived. It is, however, hypothesized from a comparison of results obtained with GRE and SE variants of the multiple-quantum sequence and substantial inherent diffusion weighting that major amounts from intravascular contributions to the functional contrast are suppressed. Addi-

tional experiments are strongly advocated for further investigation of this issue.

ACKNOWLEDGMENTS

The authors thank Toralf Mildner and Michael von Mengershausen for helpful discussions and Mandy Naumann, Annett Wiedemann, and Simone Wipper for experimental support. We are grateful to Prof. D. Yves von Cramon for thoughtful comments regarding the content of the manuscript.

REFERENCES

1. Warren WS, Richter W, Andreotti A, Farmer BT. Generation of impossible cross-peaks between bulk water and biomolecules in solution NMR. Science 1993;262:2005–2009.
2. Richter W, Lee S, Warren WS, He Q. Imaging with intermolecular multiple-quantum coherences in solution NMR. Science 1995;267: 654–657.
3. Warren WS, Ahn S, Mescher M, Garwood M, Ugurbil K, Richter W, Rizi R, Hopkins J, Leigh JS. MR imaging contrast enhancement based on intermolecular zero quantum coherences. Science 1998;281:247–251.
4. Bowtell R, Bowley RM, Glover P. Multiple spin echoes in liquids in a high magnetic field. J Magn Reson 1990;88:643–651.
5. Richter W, Warren WS. Intermolecular multiple quantum coherences in liquids. Conc Magn Reson 2000;12:396–409.
6. Zhong J, Chen Z, Kwok E, Kennedy S. Enhanced sensitivity to molecular diffusion with intermolecular double-quantum coherences: Implications and potential applications. Magn Reson Imaging 2001;19:33–39.
7. Mori S, Hurd RE, van Zijl PCM. Imaging of shifted stimulated echoes and multiple spin echoes. Magn Reson Med 1997;37:336–340.
8. Richter W, Richter M, Warren WS, Merkle H, Andersen P. Adriany G, Ugurbil K. Functional magnetic resonance imaging with intermolecular multiple-quantum coherences. Magn Reson Imaging 2000;18:489–494.
9. Zhong J, Chen Z, Kwok E. In vivo intermolecular double-quantum imaging on a clinical 1.5 T MR scanner. Magn Reson Med 43:335–341, 2000.
10. Zhong J, Chen Z, Kwok E. New image contrast mechanism in intermolecular double-quantum coherence in human MR imaging. J Magn Reson Imaging 2000;12:311–320.
11. Zhong J, Kwok E, Chen Z. fMRI of auditory stimulation with intermolecular double-quantum coherences (iDQCs) at 1.5 T. Magn Reson Med 2001;45:356–364.
12. Zhong J, Chen Z, Kwok E, Kennedy S, You Z. Optimizing of blood oxygenation level-dependent sensitivity in magnetic resonance imaging using intermolecular double-quantum coherence. J Magn Reson Imaging 2002;16:733–740.
13. Rizi RR, Ahn S, Alsop DC, Garrett-Roe S, Mescher M, Richter W, Schnall MD, Leigh JS, Warren WS. Intermolecular zero-quantum coherence imaging of the human brain. Magn Reson Med 2000;43:627–632.
14. Gutteridge S, Ramanathan C, Bowtell R. Mapping the absolute value of M_0 using dipolar field effects. Magn Reson Med 2002;47:871–879.
15. Capuani S, Hagberg G, Fasano F, Indovina I, Castriota-Scandberg A, Maraviglia B. In vivo multiple spin echoes imaging of trabecular bone on a clinical 1.5 T MR scanner Magn Reson Imaging 2002;20:623–629.
16. Chin CL, Tang X, Bouchard LS, Saha PK, Warren WS, Wehrli FW. Isolating quantum coherences in structural imaging using intermolecular double-quantum coherence MRI. J Magn Reson 2003;165:309–314.
17. Kennedy SD, Zhong J. Diffusion measurements free of motion artifacts using intermolecular dipole-dipole interactions. Magn Reson Med 2004;52:1–6.
18. Mansfield P. Multi-planar image formation using NMR spin echoes. J Phys C 1977;10:L55–L58.
19. Jochimsen TH, von Mengershausen M. ODIN—object-oriented development interface for NMR. J Magn Reson 2004;170: 67–78. URL http://od1n.sourceforge.net
20. Bax A, de Jong PG, Mehlkopf AF, Smidt J. Separation of the different orders of NMR triple-quantum transitions by the use of pulsed field gradients. Chem Phys Lett 1980;69:567–570.
21. Chen Z, Zheng S, Zhong J. Optimal RF flip angles for multiple spin-echoes and iMQCs of different orders with the CRAZED pulse sequence. Chem Phys Lett 2001;347:143–148.
22. Marques JP, Bowtell R. Optimizing the sequence parameters for double-quantum CRAZED imaging. Magn Reson Med 2004;51:148–157.
23. Deville G, Bernier M, Delrieux JM. NMR multiple echoes observed in solid ^{3}He. Phys Rev B 1979;19:5666–5688.
24. Norris DG. Reduced power multislice MDEFT imaging. J Magn Reson Imaging 2000;11:445–451.
25. Lohmann G, Müller K, Bosch V, Mentzel H, Hessler S, Chen L, Zysset S, von Cramon DY. Lipsia—a new software system for the evaluation of functional magnetic resonance images of the human brain. Comput Med Imaging Graph 2001;25:449–457.
26. Mugler JP, Brookeman JR. Three-dimensional magnetization-prepared rapid gradient-echo imaging (3D MP RAGE). Magn Reson Med 1990; 15:152–157.
27. Friston KJ. Statistical parametric maps in functional imaging: A general linear approach. Hum Brain Mapp 1994;2:189–210.
28. Wansapura JP, Holland SK, Dunn RS, Ball WS. NMR relaxation times in the human brain at 3.0 Tesla. J Magn Reson Imaging 1999;9:531–538.
29. Chen Z, Chen Z, Zhong J. Quantitative study of longitudinal relaxation related to intermolecular dipolar interactions in solution NMR. Chem Phys Lett 2001;333:126–132.
30. Jochimsen TH, Norris DG, Mildner T, Möller HE. Quantifying the intra- and extravascular contributions to spin-echo fMRI at 3 tesla. Magn Reson Med 2004;52:724–732.
31. Le Bihan D, Breton E, Lallemand D, Grenier P, Cabanis E, Laval-Jeantet M. MR imaging of intravoxel incoherent motions: application to diffusion and perfusion in neurologic disorders. Radiology 1986;161:401–407.
32. Maki JH, MacFall JR, Johnson GA. The use of gradient flow compensation to separate diffusion and microcirculatory flow in MRI. Magn Reson Med 1991;17:95–107.
33. Kennan RP, Gao JH, Zhong J, Gore JC. A general model of microcirculatory blood flow effects in gradient sensitized MRI. Med Phys 1994; 21:539–545.
34. Boxerman JL, Bandettini PA, Kwong KK, Baker JR, Davis TL, Rosen BR, Weisskoff RM. The intravascular contribution to fMRI signal change: Monte Carlo modeling and diffusion-weighted studies *in vivo*. Magn Reson Med 1995;34:4–10.
35. Song AW, Wong EC, Tan SG, Hyde JS. Diffusion weighted fMRI at 1.5 T. Magn Reson Med 1996;35:155–158.
36. Robyr P, Bowtell R. Measuring diffusion in liquids with a single gradient pulse. J Magn Reson A 1996;121:206–208.
37. Ardelean I, Kimmich R. Diffusion measurements with the pulsed gradient nonlinear spin echo method. J Chem Phys 2000;112:5275–5280.
38. Loureiro de Sousa P, Gounot D, Grucker D. Flow effects in long-range dipolar field MRI. J Magn Reson 2003;162:356–363.